Space Science Reviews
DOI 10.1007/s11214-017-0384-2
Preprint: May not contain full edited content of published article

# Design and Performance of the ICON EUV Spectrograph

**Martin M. Sirk · Eric J. Korpela · Yuzo Ishikawa · Jerry Edelstein · Edward H. Wishnow · Christopher Smith · Jeremy McCauley · Jason B. McPhate · James Curtis · Travis Curtis · Steven R. Gibson · Sharon Jelinsky · Jeffrey A. Lynn · Mario Marckwordt · Nathan Miller · Michael Raffanti · William Van Shourt · Andrew W. Stephan · Thomas J. Immel**

Submitted: 7 September 2016 / Accepted: 24 May 2017


**Abstract** We present the design, implementation, and on-ground performance measurements of the Ionospheric Connection Explorer EUV spectrometer, *ICON EUV*, a wide field ($17° \times 12°$) extreme ultraviolet (EUV) imaging spectrograph designed to observe the lower ionosphere at tangent altitudes between 100 and 500 km. The primary targets of the spectrometer, which has a spectral range of 54–88 nm, are the O II emission lines at 61.6 nm and 83.4 nm. Its design, using a single optical element, permits a $0\overset{\circ}{.}26$ imaging resolution perpendicular to the spectral dispersion direction with a large (12°) acceptance parallel to the dispersion direction while providing a slit-width dominated spectral resolution of $R \sim 25$ at 58.4 nm. Pre-flight calibration shows that the instrument has met all of the science performance requirements.

**Keywords** Extreme Ultraviolet · Instrumentation · Ionosphere · Spectrograph

## 1 Introduction

### 1.1 *ICON* Mission

The *ICON* observatory is a NASA Explorer mission that will study the boundary between Earth and space to understand the physical connection between the biosphere and outer space. This connection is made in the ionosphere, long known to respond to space weather driven by the Sun. Studies in the 21st century have revealed that energy and momentum of our atmosphere have effects of similar magnitude on the ionosphere. *ICON's* goal is to measure the relative impacts of these drivers.

*ICON* will observe the ionosphere from a circular orbit at an altitude of 575 km employing a suite of four instruments. An orbital inclination of 27° allows rapid access via precession to all available low

M. M. Sirk, E. J. Korpela, Y. Ishikawa, J. Edelstein, E. Wishnow, J. McCauley, J. B. McPhate, J. Curtis, T. Curtis, S. R. Gibson, J. A. Lynn, M. Marckwordt, N. Miller, M. Raffanti, W. V. Shourt, T. Immel
University of California, Space Sciences Laboratory, Berkeley CA, USA
E-mail: sirk@ssl.berkeley.edu

S. Jelinsky
Lawrence Berkeley National Laboratory, Berkeley, CA, USA

A. W. Stephan
Naval Research Laboratory, Washington, DC, USA

and middle latitudes, longitudes, and local time. Emission line features in the EUV and FUV will be measured by two co-aligned spectrographs to yield ion density altitude profiles. Ionosphere winds and temperature will be determined with an interferometer working at visible wavelengths, while ion velocity at the observatory will be determined with an ion drift meter. The observatory is scheduled for launch on a Pegasus vehicle in November 2017. A detailed overview of the *ICON* mission is presented in this volume by Immel et al. (2017)[1]. The *ICON EUV* spectrometer is the subject of this paper. The other instruments are discussed in separate papers (also this volume)[2,3,4].

### 1.2 *ICON EUV*

The existence of EUV emission from singly ionized oxygen ($O^+$) in the ionosphere of the Earth has long been known and is a useful diagnostic of the ionization state and density of the lower ionosphere[5]. The brightest of the OII dayglow line complexes in the EUV is the 83.4 nm resonance triplet resulting from transition from the $2s2p^4\,^4P$ excited states to the $2p^3\,^4S^o$ ground state. The high population of nearby ions in the ground state causes a high probability that an emitted photon from this transition will be reabsorbed, resulting in a high optical depth in this transition. This can make it difficult to disentangle optical depth effects from illumination and ion density effects when attempting to determine density of the $O^+$ ion. The nearby triplet at 61.6 nm from the $3s\ ^2P$ state to the $2p^3\,^2D^o$ state, is optically thin. In principle, the two taken together can be used to more directly obtain the ion density and illumination source function than the 83.4 nm emission alone[6]. Similar transitions at 67.3 nm and 71.8 nm could be used to supplement this analysis.

The *ICON EUV* spectrometer has been designed to perform wide field altitude profilometry of the region surrounding the peak $O^+$ densities in the lower ionosphere, at tangent altitudes between 100 and 500 km with a vertical resolution of 20 km, and a horizontal resolution of 500 km (Figure 1. See also Figure 18 of Immel et al. (2017), this volume[1]). In normal observing mode, *ICON EUV* will be pointed generally north perpendicular to the spacecraft velocity vector and take 12 s exposures. Each observation will image a 12° wide (spectral) by 17° high (imaging) wedge of the atmosphere from which daytime ion density altitude profiles from 100 to 500 km can be determined (illustrated in Figure 2). Because the spacecraft motion during 12 s results in a shift of only 0°.76 along the orbit (small compared to the 12° field of view), each exposure is effectively a snapshot. Required sensitivity of 7.4 Rayleigh at 61.7nm and 30 Rayleigh at 83.4 nm were determined based simulated model inversions of the altitude profiles to derive the $O^+$ density versus altitude[7,8]. This minimum sensitivity is 10% of the maximum ionospheric density emission. The primary design requirements relate to obtaining the sensitivity and angular resolution necessary to determine the maximum ion density of the F2 layer and the altitude of the maximum density using the 61.6 nm and 83.4 nm emission while rejecting interference from scattered HI Ly$\alpha$ and the nearby HeI 58.4 nm line. Table 1 shows the primary design requirements needed to achieve these goals. End of life requirements are based upon worst case sensitivity losses in the microchannel plate detector and continuous low-rate deposition of hydrocarbon contamination on the instrument diffraction grating. Total end of life efficiency loss under these assumptions is 60% from "pristine" conditions on receipt of the optics and microchannel plates. Actual degradation will be tracked through on-orbit calibration activities.

## 2 Description of Instrument

The *ICON EUV* instrument is a diffuse imaging spectrograph consisting of an entrance aperture, a diffraction grating, and a bare microchannel plate (MCP) detector. The grating was manufactured by Horiba Jobin Yvon and delivered with a 40 nm thick coating of Cr. To enhance reflectivity in the EUV additional layers of Ir (20 nm) and $B_4C$ (10 nm) were applied by Reflective X-ray Optics LLC. The MCP detector

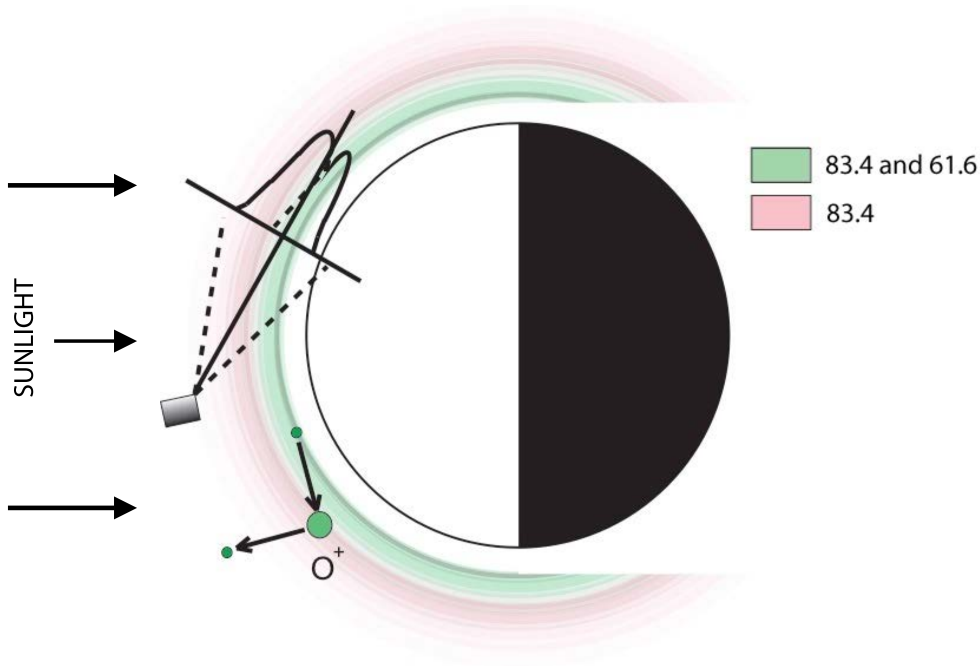


**Fig. 1** Illustration of the *ICON EUV* observing geometry. Space craft motion is towards the reader. Vertical (imaging) field of view is 17°.3 and is demarcated by dashed lines. Horizontal (spectral) field of view is 12°.1 (plus 0°.76 caused by 12 s of space craft motion). Height of the atmosphere is exaggerated by 5x.

**Table 1** *ICON EUV* design requirements.

| | Requirement | Achieved |
|---|---|---|
| Spectral Resolution[a] | 4.2 nm | 2.4 nm |
| Angular Imaging Resolution[b] | 0°.45 | 0°.26 |
| $3\sigma$ Minimum Measurable Flux[c] | | |
| – at 61.6 nm | <7.4 R | 3.3 R (BOL[d]) |
| | | 6.6 R (EOL[e]) |
| – at 83.4 nm | <30 R | 3.7 R (BOL) |
| | | 5.8 R (EOL) |
| Vertical Field-of-View | >14° | 17°.3 |

[a]90% Enclosed Energy Width at 58.4 nm.
[b]Full Width Half Maximum.
[c]in a 60 second exposure.
[d]Beginning of Mission Life.
[e]End of Mission Life (estimated).

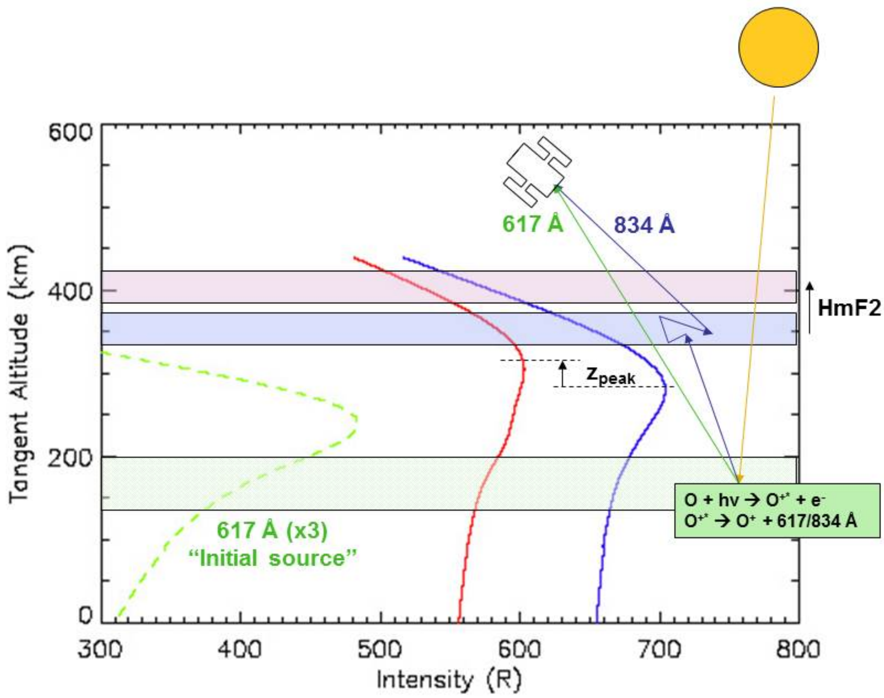


**Fig. 2** This schematic shows the key elements of the approach used to infer the daytime ionosphere from the *ICON EUV* measurements.[7, 8] The $O^+$ in the ionospheric F-layer, represented here as a discrete slab for two different ionospheric profiles with hmF2 = 350 km (blue) and hmF2 = 400 km (red), scatters the 83.4 nm photons generated in the lower thermosphere, represented by the green layer centered near 170 km. The brightness of this photon source that illuminates the ionosphere from below is captured in ICON EUV measurement of the 61.7 nm emission, while the two simulated 83.4 nm emission profiles demonstrate the change in the shape as well as the magnitude and height ($z_{peak}$) of the peak that would be measured as a result of these two different ionospheric profiles. For these specific simulations, an ionospheric Chapman layer is used with the same NmF2 = 1.0e6 $cm^{-3}$.

and spectrograph were both designed and assembled at the Space Sciences Laboratory (SSL) at the University of California Berkeley Campus. The design is patterned after the successful *SPEAR* mission[9, 10]. The spectrograph housing is a hermetic enclosure measuring $\sim$ 38 by 21 by 34 cm and has a mass of 10 kg. Figure 3 is a side view of the instrument including its mounting feet.

Because contamination is a significant concern for EUV instruments, the entire instrument housing is built as a vacuum cavity. A sealed one-shot door in front of the instrument is opened in orbit, or in a vacuum chamber, to allow evacuation and allow light to enter. For ground operations, the instrument can be maintained at high vacuum by attaching a vacuum pump to the instrument's pumping port. During operations for which pumping is not possible, the instrument can be purged with clean dry nitrogen through a purge port. The purge gas escapes through $\sim$1 psi poppet valves that are also used to release pressure during ascent. For short durations, the instrument can be back-filled with dry nitrogen and sealed to prevent contamination.

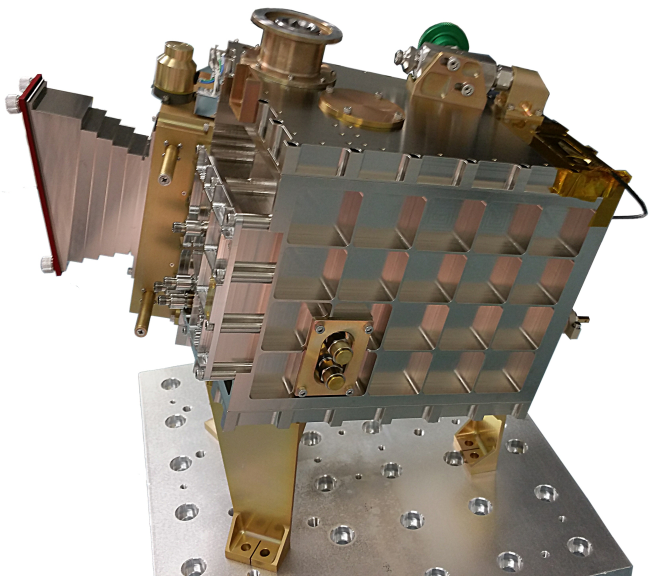

**Fig. 3** Spectrograph housing. Visible are the external slit baffle at far left, the door mechanism at left (gold), and the MCP detector at near left. One grating adjustment screw is visible at far right. Flight electronics and harnessing are absent. See Figure 10 for a view inside the housing.

During operation EUV radiation from the sky enters the 0.90 by 40.0 mm slit, illuminates a 50 by 95 mm toroidal figure, ion-blazed (lamellar profile), holographically ruled diffraction grating [11], and is then focused by the grating onto a 19 by 54 mm cross delay line MCP detector with a spatial resolution of 90 $\mu$m in the spectral direction, and 160 $\mu$m in the imaging direction[12]. On-board electronics digitize the photon events into an image 160 pixels wide in the spectral dimension, and 101 pixels tall in the imaging dimension. The field of view is determined by internal and external baffles, and the grating dimensions. The optical scheme provides imaging without using a separate telescope optic. In the spectral direction, the toroidal grating focuses an image of the slit onto the detector while in the imaging direction the toroid focuses at infinity resulting in a spectral image where each row is a spectrum from a horizontal slice of the sky 12° wide, and each column a vertical angular intensity profile at a given wavelength. A diagram of the focusing properties of the grating is shown as Figure 4. The grating is coated with a special EUV-optimized, low stress $B_4C$/Ir/Cr multilayer[13]. The grating parameters are listed in Table 2 and the MCP detector parameters in Table 3.

## 3 Calibrations

The single aperture, optic, and detector simplicity of the instrument inspired this calibration strategy:

1. Separately characterize the performance of the diffraction grating (coating efficiency, order efficiencies) and the detector quantum efficiency (QE) at discrete wavelengths.
2. For the integrated instrument determine the absolute throughput, wavelength scale, resolution, field of view, and in-, and out-of-band scattering levels at discrete wavelengths.

**Table 2** Diffraction grating parameters and measured order efficiencies ($\eta^a$).

| Item | Specification | Notes/Ref. |
|---|---|---|
| Grating Substrate | Fused Silica | |
| Grating Dimensions | 100, 55 mm | Imaging, Spectral |
| Radii of Curvature | 335.5, 175.8 mm | Imaging, Spectral[11] |
| Useful Ruled Area | 95 x 50 mm | Ref[11] |
| Groove Density | 3000.28 $\pm$0.2 $mm^{-1}$ | Ref[11] |
| $\alpha_{central ray}$ | $13\overset{\circ}{.}67$ | Ref[11] |
| Cr Thickness | 40 nm | Ref[11] |
| Ir Thickness | 20 nm | Ref[13] |
| $B_4C$ Thickness | 10 nm | Ref[13] |
| $-1$ Order $\eta$ | 41.75% $\pm$0.19 | at 58.4 nm |
| 0 Order $\eta$ | 0.81% $\pm$0.066 | at 58.4 nm |
| $+1$ Order $\eta$ | 33.38% $\pm$0.63 | at 58.4 nm |
| $+2$ Order $\eta$ | 1.40% $\pm$0.90 | at 58.4 nm |

[a]Order efficiencies are relative to the reflective efficiency of the $B_4C$-Ir-Cr coating sample supplied with the grating.

**Table 3** Microchannel Plate Detector Parameters.

| Item | Specification | Notes |
|---|---|---|
| MCP Size | 60, 25 mm | Imaging, Spectral |
| Active Area | 54, 19 mm | Imaging, Spectral |
| Image Size | 101, 160 pixels[a] | Imaging, Spectral |
| Plate Thickness[b] | 1.0 mm | 80:1 h/d ratio |
| Pore Diameter | 12.5 $\mu$m | |
| Pore Pitch | 15 $\mu$m | |
| Pore Bias[c] | 13° | Parallel to short dimension |
| Resolution | 160 $\mu$m | Imaging @ 1 pC gain |
| Resolution | 90 $\mu$m | Spectral @ 1 pC gain |
| Electrode material | NiCr | |

[a]Pixel sizes are set by flight electronics.
[b]Three plates are stacked in a "Z" configuration.
[c]Top of pores on uppermost plate are tilted towards the slit (see Figure 10).

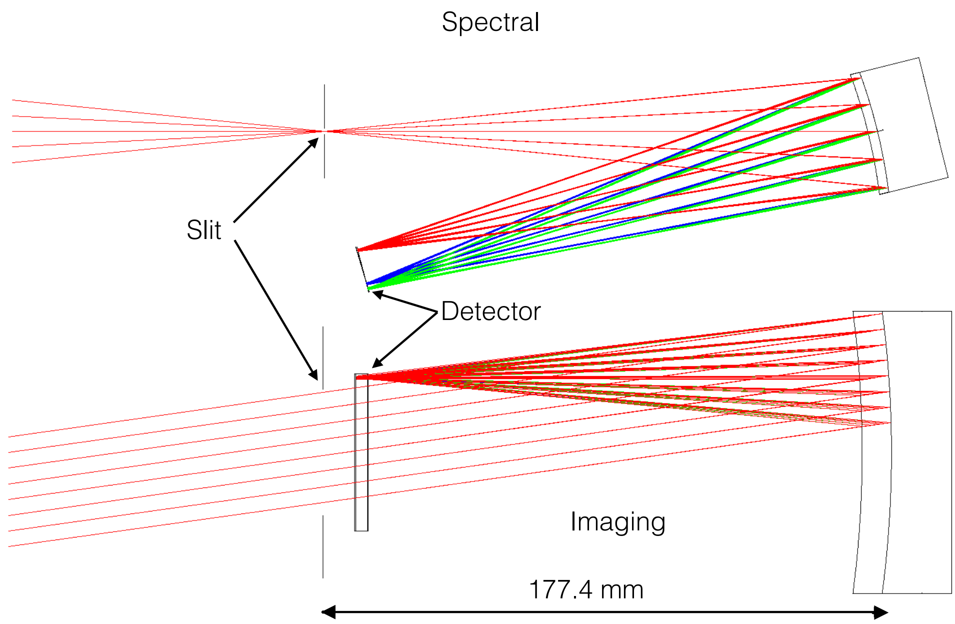


**Fig. 4** Schematic diagram showing how light of three wavelengths (58.4, 61.6, and 83.4 nm, green, blue, and red, respectively) from the entire 12° wide spectral field of view is focused onto detector along the dispersion direction (top, and Figure 10), and how collimated, in-band light from a particular altitude angle is focused onto one row on the detector in the imaging direction (bottom). Slit width is exaggerated by a factor of 2 in top panel.

3. Use efficiency models provided by the diffraction grating and optical coating manufactures that are scaled to SSL measurements to predict performance at other wavelengths.
4. On–orbit, use Moon pointings of reflected Solar EUV light to verify optical alignment, focus, and throughput. Use downward-looking (nadir) pointings to make flat field and vignetting maps.

All calibrations were performed at the SSL small vacuum tank facility.[14] A gas discharge source and monochromator were employed to provide in-, and out-of-band, discrete wavelength EUV radiation. A 4-axis manipulator allowed for the testing of both individual components and the complete instrument at various translational and rotational configurations.

Two different modes of illumination were required to fully characterize the optical performance of the spectrograph. Slightly divergent pencil beams (about $f/150$) 1 to 5 mm in diameter proved ideal for field of view, absolute QE determinations and out-of-band scattering levels. For optical alignment, and spectral and imaging resolution determinations the system was tested using an optical simulator consisting of a convex sphere and concave toroid pair of mirrors (with the toroid having similar radii of curvature to that of the spectrometer grating). The simulator forms a converging cylindrical beam that mimics that arising from a uniformly luminous patch of the sky that is focused to a line ≈0.3 mm wide at the spectrometer slit[15]. The simulator is illuminated with pencil beam radiation from the laboratory monochromator operating in 0th order, so that multi-wavelength measurements are made simultaneously.

### 3.1 Optical Alignment and Wavelength Scale

The optical simulator was used to direct EUV light from He-Ne and O gas discharge sources through the center of the entrance slit towards the center of the diffraction grating (on-axis illumination). Optical alignment was achieved in vacuum by turning the three grating mount fine-adjustment screws via stepper motors and minimizing the spot sizes on the detector images in both the imaging and spectral dimensions. Once aligned, seven emission lines were identified and used for determining the wavelength scale (see Figure 5). In the case of blended O lines effective wavelengths are assigned using weighted averages based on values from Kelly and Palumbo (1973)[16] and NIST[17]. A second order polynomial fit is performed to determine wavelength as a function of detector position and shows a RMS residual of 0.45Å (0.045 nm). We show the residuals and the dispersion relation in Figure 6. The uncertainties in the fit are dominated by uncertainties in the effective wavelengths (∼0.3Å ), and small shifts in measured pixel position caused by localized detector distortion (about 0.1 pixel or 0.2Å ).

### 3.2 Field of View

The ultimate sensitivity of the instrument at a given wavelength is the product of the instrument throughput efficiency and the etendue (the product of the entrance aperture area and the solid angle of the sky visible by the grating). The slit dimensions were measured with a microscope on a fine micrometer stage and are 0.904 mm wide, and 40.0 mm long. The geometrical area is 0.3616 ±0.0016 $cm^2$. The angular field of view was determined by shining a pencil beam of 83.4 nm EUV light at 3 different positions along the slit while rotating the instrument in both pitch and yaw by known amounts. The field of view measured at FWHM is $17\overset{\circ}{.}31 \pm 0\overset{\circ}{.}1$ and $12\overset{\circ}{.}12 \pm 0\overset{\circ}{.}05$ in the imaging and spectral directions, respectively. These values correspond to a solid angle of 0.06391 ±0.00045 sr. The value determined for the imaging direction is for the center of the slit. Off-axis rays may experience vignetting and will be calibrated in orbit using time-averaged nadir pointings.

### 3.3 Absolute Photometric Throughput

The throughput determinations required several steps. First, absolute measurements were performed for the central ray at three wavelengths (58.4, 61.6, and 83.4 nm) by alternately directing pencil beams into the instrument and onto a photodiode calibrated by NIST.[18] To ensure full capture of the EUV pencil beams by the grating, the entrance slit was removed from the instrument during photometric calibrations. These measurements provide the absolute photometric sensitivity for on-axis light incident at the center of the grating.

Second, measurements were made relative to the central ray by rotating and translating the instrument to illuminate the grating at approximately flight-like conditions. In Figure 7 we show the angular response relative to the central ray for both the spectral and imaging angles. The average value of each of these images (excluding regions beyond the measured field of view) gives sensitivities relative to the central ray of 97.8% and 105% at 58.4 nm and 83.4 nm, respectively. The displacement of peak sensitivity towards positive angles is an expected consequence of the MCP pore bias angle which is tilted 13° parallel to the

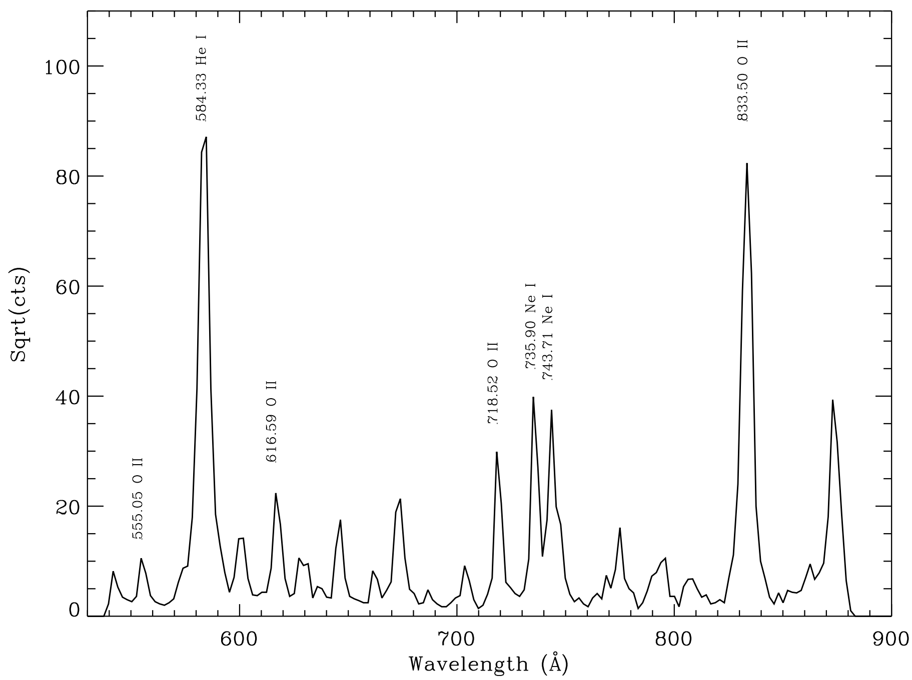


**Fig. 5** *ICON EUV* spectrum created by adding individual spectra of He-Ne and O obtained with the optical simulator. Labeled lines are used for wavelength calibration.

spectral direction. Rays strike the MCP detector at up to $\pm$ 8.6° from normal along this dimension. See Figure 4 for the ray geometry.

The third step is to determine the sensitivity at other wavelengths. This requires knowing the wavelength dependent efficiencies of the diffraction grating, the $B_4C$/Ir/Cr coating, and the flight detector. Measurements were performed for each of these components at discrete wavelengths at SSL. Linear interpolation for intermediate values of detector QE proved adequate. For the coating efficiency and the diffraction grating relative order efficiency we use the theoretical performance (based on the measured groove profile) provided by the manufacturers[13,11], multiply them, and scale the resulting curve to match the Berkeley measurements. We present the component efficiencies in the upper panel of Figure 8. The product of these curves gives the predicted throughput which we compare to the Berkeley measurements of instrument efficiency in the lower panel of Figure 8.

The predicted instrument efficiency is about 20% greater than the three SSL measurements shown in Figure 8. We investigated these differences using a reference MCP detector calibrated with a second NIST photodiode. The two diodes were measured side by side and agree to within 5%. The instrument responses we determined using the first photodiode agreed with those derived from the reference detector to within 11%. We were careful to account for obscuration of the flight detector from an ion repelling

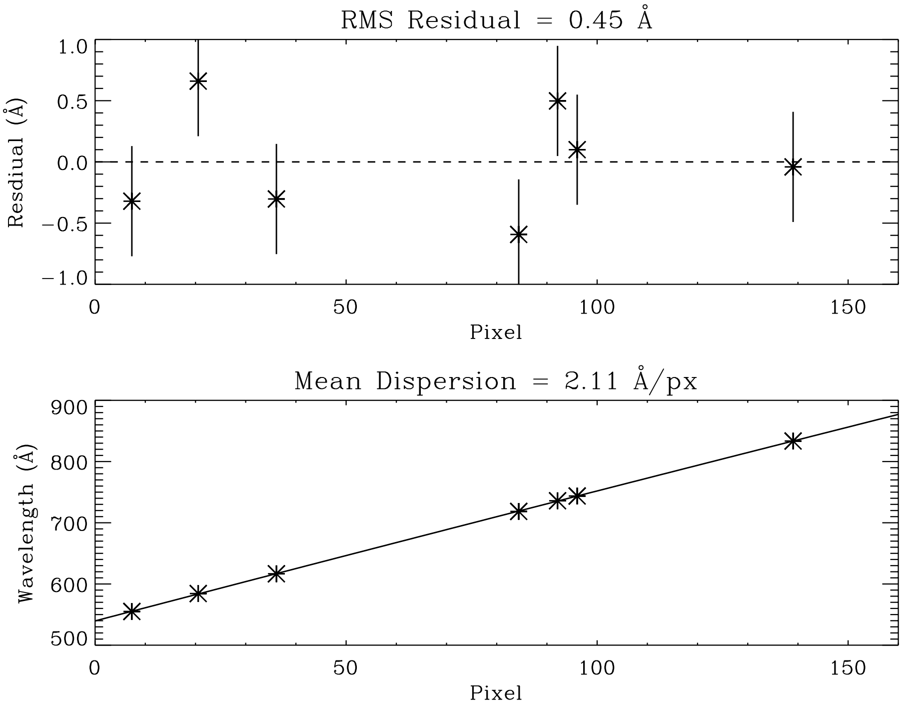


**Fig. 6** Second order polynomial fit wavelength residual (top) and dispersion relation (bottom).

grid in our efficiency comparisons. We cannot account for the 20% difference between the measured and predicted efficiency, but believe that the SSL instrument measurements of throughput are accurate to within an internal uncertainty of 11%.

Accurate knowledge of the uncertainties in the absolute photometric throughput at the wavelengths of interest, namely the OII emission lines at 61.6 nm and 83.4 nm (and, potentially, 67.3 nm and 71.8 nm), is required by the plasma density inversion models. We combine the reference photodiode uncertainty of 7% quoted by NIST[18] and our internal measurement uncertainty of 11% in quadrature to get 13% (the error bars plotted in the lower panel of Figure 8). For throughput at other wavelengths based on interpolations we add an additional error of 5% in quadrature to yield an uncertainty of 14%. These values are our best estimate of the systematic uncertainty in the derived line fluxes.

## 3.4 Spectral and Imaging Resolution

To quantify the focusing properties of the spectrograph required fully illuminating the grating as well as the entrance slit. The optical simulator fully illuminates the grating, but produces a line-image only 1/3 (0.3 mm) as wide as the slit. Hence, small lateral motions of the simulator spherical mirror (slit scans) were required to create synthetic images of a fully illuminated entrance aperture. A set of slit scans obtained at

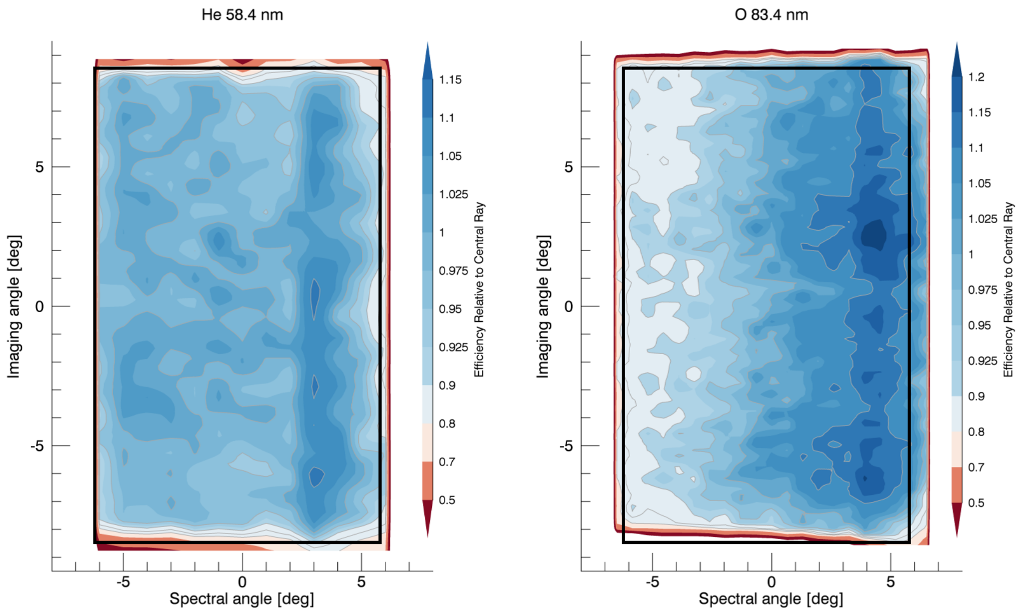


**Fig. 7** Angular sensitivity maps normalized to central ray for 58.4 nm (left) and 83.4 nm (right). The relative uncertainty at any given point on the maps is $\sim$5%. Heavy black lines demarcate the measured field of view with all baffles installed.

different imaging angles and then added together provides our best proxy for flight-like illumination. In Figure 9 we present the integrated image from the oxygen discharge source, and we show three spectra each of He-Ne, and O extracted at the top, middle, and bottom of the detector image. Small changes in line shape and position are evident. Combining the synthetic O spectrum with a similar one obtained with He-Ne we find a resolution in the imaging direction of $0.^\circ26$ at FWHM. In the spectral dimension the resolution is slit-limited—emission features appear somewhat flat-topped. We find a typical line-width of 2.4 nm at 90% enclosed energy width which corresponds to R $\sim$ 25.

We also obtained spectra during thermal vacuum testing to verify optical stability. Temperature excursions ranged from 10 C to 40 C. No significant shift in position of spectral features was observed, nor any degradation of the spectral and imaging resolutions[15].

### 3.5 Scattered and Stray Light

Most spectrographs are compromised to some degree by unwanted light typically caused by the diffraction grating scattering both in-, and out-of-band light, light from orders other than those of interest, and stray light that bounces off one or more interior surfaces and ultimately lands on the detector. When EUV light within the field of view is directed through the *ICON EUV* entrance aperture the holographically ruled gratings with square-wave groove profile[11] shows insignificant ($<$ 0.025%) scattering in-band at 83.4 nm, and out-of-band at 121.6 nm (Ly$\alpha$ ). However, when Ly$\alpha$ light from beyond the field of view is directed through the aperture it can scatter from one or more baffles directly, or reflect off the grating in several different orders and then scatter from baffles. We measured significant scatter counts

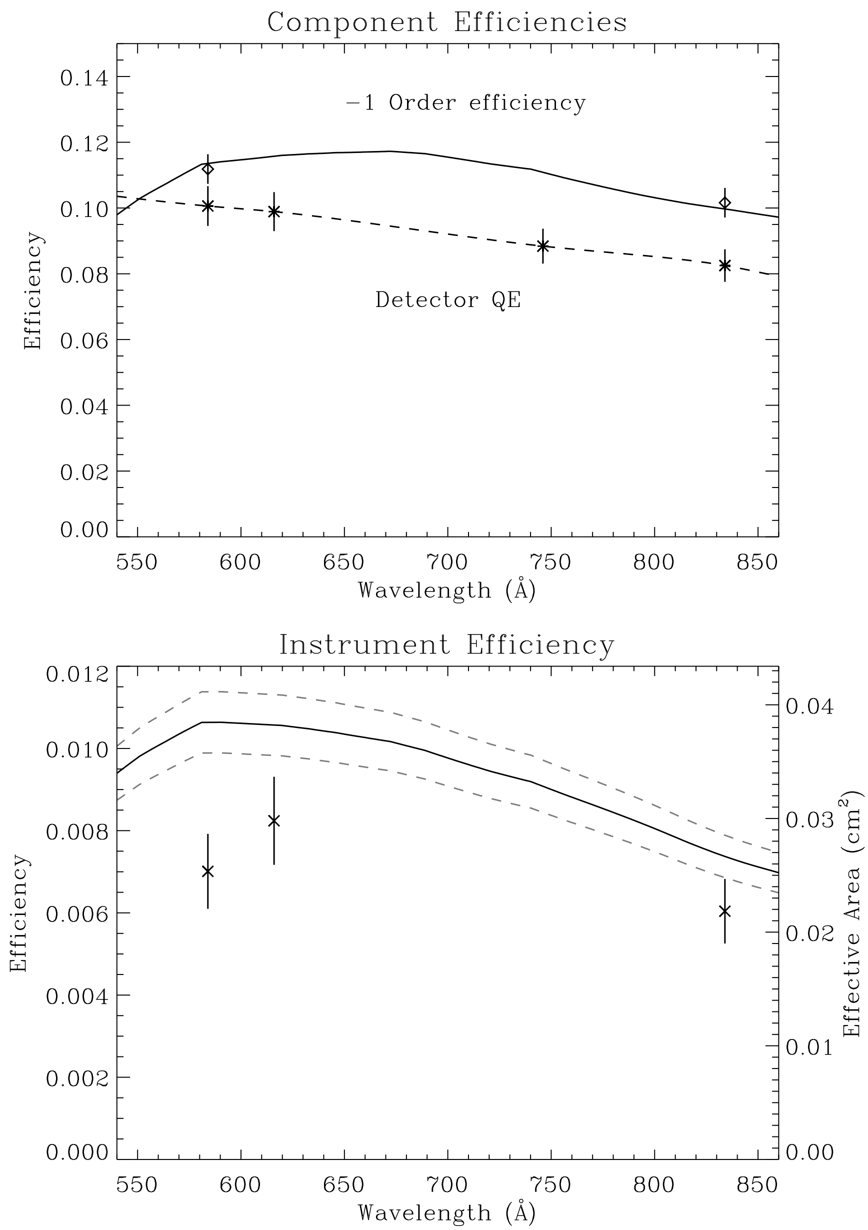


**Fig. 8** Component (upper panel) and instrument (lower panel) efficiencies. The predicted instrument efficiency is the product of the two component curves and is plotted in the lower panel (solid line) with its 1 σ uncertainty (dashed lines). In both panels the plotted symbols are Berkeley SSL measurements of absolute throughput. The uncertainties are discussed in the text.

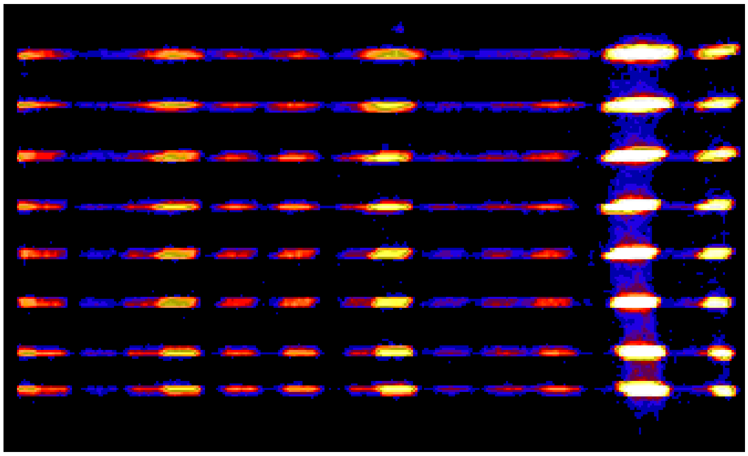

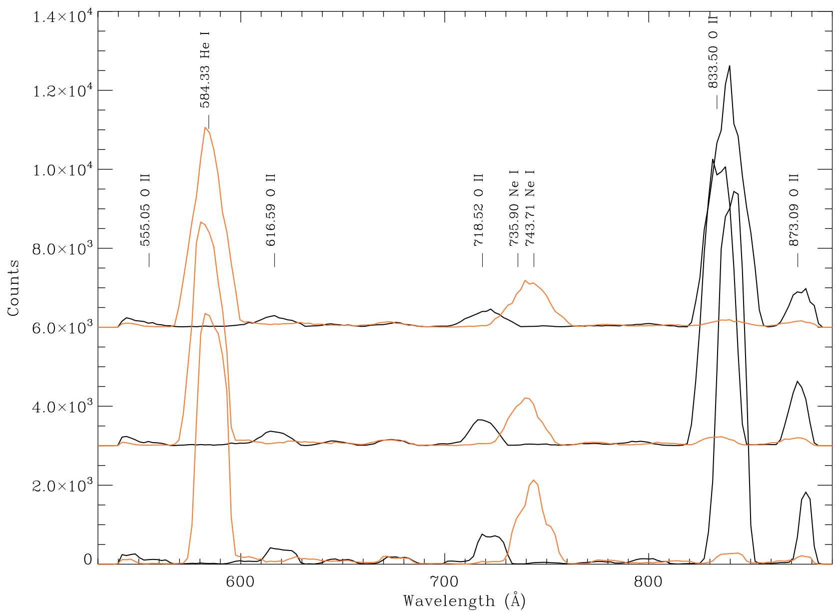


**Fig. 9** Oxygen spectrum detector image created by adding 8 different slit scans obtained at various image angles (top panel). Data have been log-scaled to emphasize faint features. Lower panel shows three spectra extracted from Oxygen (black) and He-Ne (red) images at off axis imaging angles that correspond to the uppermost, center, and lowermost scans of the image above. Small changes in line shape and position are evident.

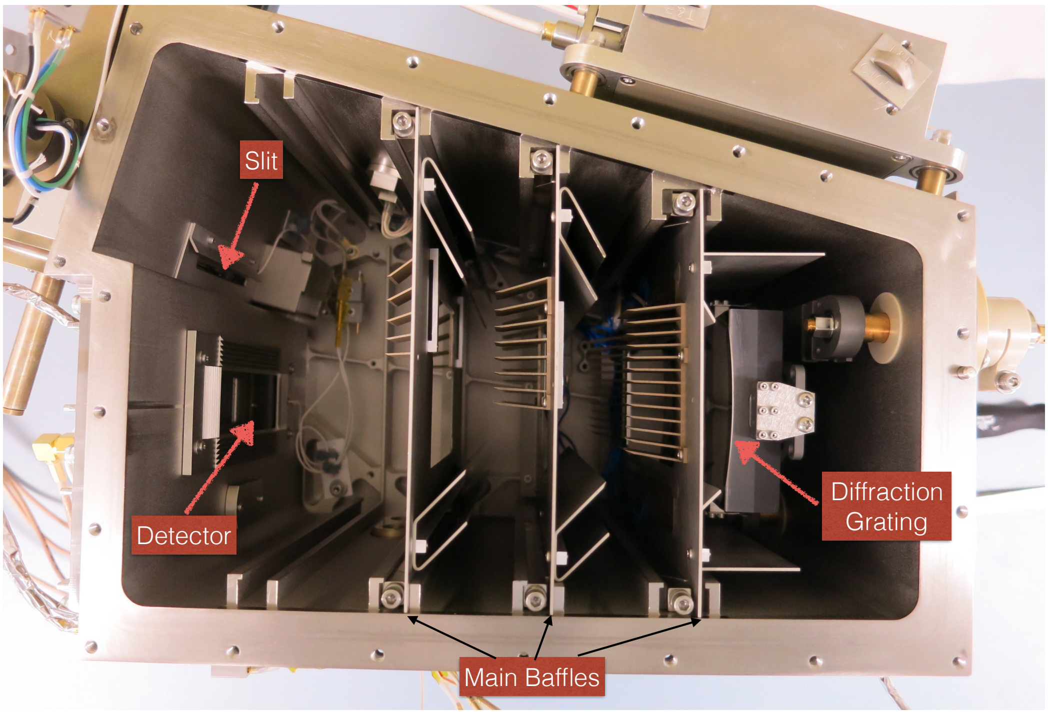


**Fig. 10** Top view into the *ICON EUV* housing showing relative location of principle components. Entrance slit and detector are at upper, and lower left, respectively. Grating is at right. Three of the four baffle sets are installed. The chevrons directed toward the grating are knife-edged to prevent glints and trap light from unwanted orders in the spectral direction. The knife-edged vanes directed towards the detector shadow the main baffle plates (vertical sheets seen nearly edge-on) from direct illumination in the imaging direction. The exterior baffle can been seen in Figure 3.

at the detector ($\approx 19\ \mathrm{cm}^{-2}$ per $1.5 \times 10^6$ Ly $\alpha$ input photons) from off-axis light in both the spectral and imaging planes. We define scatter counts as the count rate above dark background integrated over the entire detector surface.

Several modifications were required to reduce the scattered light to acceptable levels. In the spectral direction, baffle edges were sharpened to knife-edges to prevent glints. Outside of the slit, one baffle was extended slightly to prevent direct illumination of a baffle facet close to the grating. In the imaging direction additional baffles were fabricated to fully shadow existing baffles where knife-edging was insufficient. Figure 10 is a top-down view into the *ICON EUV* housing showing the baffle placement.

The measured scattering level was reduced by more than a factor of 13 ($\approx 1.4\ \mathrm{cm}^{-2}$ per $1.5 \times 10^6$ Ly $\alpha$ input photons) to a level which should not compromise science observations. Based on our experience with this and other instruments[19], we encourage others to carefully consider stray light effects early in the instrument design cycle.

## 4 In-flight calibration

Once in orbit, *ICON EUV* is expected to undergo changes in its spectral response. Anticipated impacts include contamination and reduced gain and count loss due to charge depletion of the microchannel plates in regions of high count rate, primarily near the peak intensity of 83.4 nm. Such changes in instrument response could disrupt the determination of peak ion density and the altitude of peak density. To combat this effect we will be performing two types of in-flight calibrations.

The first will be a monthly recalibration against the full moon. The EUV field of view will be swept across the full moon at seven evenly spaced imaging angles. Using the known EUV albedo of the moon[20] and near-concurrent EUV solar measurements[21], we will recalculate the spectral response so as to track changes.

The second will be a monthly flat-field calibration. For these calibrations the spacecraft will be oriented so that the EUV instrument boresight is pointing towards nadir with the slit oriented parallel to the spacecraft velocity vector. In this configuration any variation in the atmospheric intensity will quickly traverse along the slit. After a several hundred second exposure, each pixel will have seen essentially the same emitting regions and the resulting image can be used to determine a flat field correction at each of the science wavelengths and imaging angles.

## 5 Conclusions

The imaging and spectral resolutions are well within specifications. Detector dark background is $<0.3\ \mathrm{s}^{-1}\ \mathrm{cm}^{-2}$ and therefore negligible. In-band scattering from the grating is also negligible. Out-of-band scattering from Ly $\alpha$ has been reduced to levels that should not be problematic. The uniformity in instrument response in the imaging direction (see Figure 7) makes flux determinations straight forward. The total systematic uncertainty in instrument response is 13% for wavelengths where we have SSL measurements, and 14% for wavelengths which required interpolation.

A set of witness samples that have traveled with the grating or the instrument have had their reflectivity (at 58.4 nm and 83.4 nm) measured periodically. No signs of coating degradation or contamination are evident. The instrument has met all its design requirements.

**Acknowledgements** We thank Carl Dobson for systems support, Steve Marker for keeping the vacuum facility operational, Christopher Scholz for technical support, Paul Turin and David Pankow who provided useful advice, and two anonymous referees who provided constructive critiques. *ICON* is supported by NASA's Explorers Program through contracts NNG12FA45C and NNG12FA42I. This project utilizes data from the NIST Atomic Spectra Database.[17] Special thanks to EUVester the pug who made boring meetings practically tolerable.

## References

1. T.J. Immel, S.L. England, S.B. Mende, R.A. Heelis, J. Englert, J. Edelstein, H.U. Frey, E.R. Taylor, W.W. Craig, S.E. Harris, M. Bester, G.S. Bust, G. Crowley, J.M. Forbes, J.C. Gerard, J.M. Harlander, J.D. Huba, B. Hubert, F. Kamalbadi, J.J. Makela, A.I. Maute, I.I. Meier, C. Raftery, P. Rochus, O.H.W. Siegmund, A.W. Stephan, G.R. Swenson, S. Frey, D.l. Hysell, A. Saito, K.A. Rider, M.M. Sirk, M.H. Stevens, Space Science Reviews (2017)
2. C.R. Englert, J.M. Harlander, C.M. Brown, K.D. Marr, I.J. Miller, J.E. Stump, J. Hancock, J.Q. Peterson, J. Kumler, W.H. Morrow, T.A. Mooney, S. Ellis, S.B. Mende, S.E. Harris, M.H. Stevens, J.J. Makela, B.J. Harding, T.J. Immel, Space Science Reviews (2017). DOI 10.1007/s11214-017-0358-4
3. R.A. Heelis, R.A. Stoneback, M.D. Perdue, M.P. Depew, Z.A. Morgan, M.D. Mankey, C.R. Lippincott, L.L. Harmon, B.J. Holt, Space Science Reviews (2017)

4. S.B. Mende, H.U. Frey, K. Rider, C. Chou, S.E. Harris, O.H.W. Siegmund, S.L. England, C.W. Wilkins, W.W. Craig, P. Turin, N. Darling, T.J. Immel, J. Loicq, P. Blain, E. Syrstadt, B. Thompson, R. Burt, J. Champagne, P. Sevilla, S. Ellis, Space Science Reviews (2017). DOI 10.1007/s11214-017-0386-0
5. P.D. Feldman, D.E. Anderson, Jr., R.R. Meier, E.P. Gentieu, J. Geophys. Res. **86**, 3583 (1981). DOI 10.1029/JA086iA05p03583
6. A.W. Stephan, J.M. Picone, S.A. Budzien, R.L. Bishop, A.B. Christensen, J.H. Hecht, J. Geophys. Res. (Space Phys.) **117**, A01316 (2012). DOI 10.1029/2011JA016897
7. A.W. Stephan, J. Geophys. Res. (Space Phys.) **121**, 9284–9292 (2016). DOI 10.1002/2016JA022629
8. A.W. Stephan, E.J. Korpela, M.M. Sirk, S. England, T.J. Immel, Space Science Reviews (2017). DOI 10.1007/s11214-017-0385-1
9. J. Edelstein, K.W. Min, W. Han, E.J. Korpela, K. Nishikida, B.Y. Welsh, C. Heiles, J. Adolfo, M. Bowen, W.M. Feuerstein, K. McKee, J.T. Lim, K. Ryu, J.H. Shinn, U.W. Nam, J.H. Park, I.S. Yuk, H. Jin, K.I. Seon, D.H. Lee, E. Sim, Astrophys. J. **644**, L153 (2006). DOI 10.1086/505208
10. E.J. Korpela, J. Edelstein, P. Berg, M.S. Bowen, R. Chung, M. Feuerstein, W. Han, J.S. Hull, H. Jin, D.H. Lee, K.W. Min, U.W. Nam, K. Nishikida, J.G. Rhee, K. Ryu, K. Seon, B.Y. Welsh, I. Yuk, in *Future EUV/UV and Visible Space Astrophysics Missions and Instrumentation*, *Proc. SPIE*, vol. 4854, ed. by J. C. Blades & O. H. W. Siegmund (2003), 665. DOI 10.1117/12.459970
11. A. Liard, *Final Control Report, Grating 54900269H* (Horiba Jobin Yvon, Longjumeau Cedex, France, 2015)
12. M.W. Davis, G.R. Gladstone, T.K. Greathouse, D.C. Slater, M.H. Versteeg, K.B. Persson, G.S. Winters, S.C. Persyn, J.S. Eterno, in *UV/Optical/IR Space Telescopes and Instruments: Innovative Technologies and Concepts V*, *Proc. SPIE*, vol. 8146 (2011), 814604. DOI 10.1117/12.894274
13. D.L. Windt, *Private Communication* (Reflective X-ray Optics LLC, New York, 2015)
14. B.Y. Welsh, P. Jelinsky, R.F. Malina, in *X-ray instrumentation in astronomy II*, *Proc. SPIE*, vol. 982, ed. by L. Golub (1988). DOI 10.1117/12.948729
15. Y. Ishikawa, E. Korpela, E.R. Wishnow, M.M. Sirk, J. Curtis, J. McCauley, C. Smith, J.B. McPhate, J. Edelstein, in *Earth Observing Systems XXI*, *Proc. SPIE*, vol. 9972 (2016), 997245. DOI 10.1117/12.2238148
16. R.L. Kelly, J. Palumbo, *NRL Report No. 7599.* (1973)
17. A. Kramida, Y. Ralchenko, J. Reader, NIST ASD Team, (2015). URL http://physics.nist.gov/asd
18. R.E. Vest, Y. Barad, M.L. Furst, S. Grantham, C. Tarrio, P.S. Shaw, Adv. Space Res. **37**, 283 (2006). DOI 10.1016/j.asr.2005.02.073
19. M.M. Sirk, G.A. Gaines, E.R. Taylor, M. Sholl, W. Marchant, R. Hemphill, R.A. Kimble, T. Sasseen, M.R. Marckwordt, W. Donakowski, in *UV/EUV and Visible Space Instrumentation for Astronomy II*, *Proc. SPIE*, vol. 5164, ed. by O.H.W. Siegmund (2003), 54. DOI 10.1117/12.515601
20. B.C. Flynn, J.V. Vallerga, G.R. Gladstone, J. Edelstein, Geophys. Res. Let. **25**, 3253 (1998). DOI 10.1029/98GL02483
21. W.D. Pesnell, B.J. Thompson, P.C. Chamberlin, Sol. Phys. **275**, 3 (2012). DOI 10.1007/s11207-011-9841-3